RSC Advances

PAPER

View Article Online
View Journal | View Issue

Cite this: *RSC Adv.*, 2026, **16**, 20855

A ZIF-8-modified electrochemical biosensor for sensitive Aβ aggregation monitoring and Alzheimer's disease drug screening

Shang-Chi Chien,†[ab] Yin-Chen Chien,†[b] Hung-Ju Wang[ab] and Jung-Chih Chen *[abcde]

Alzheimer's disease (AD) is an irreversible neurodegenerative disorder driven by the abnormal aggregation of β-amyloid (Aβ) into oligomers, fibrils, and plaques. Current therapeutic strategies primarily alleviate symptoms but struggle to prevent aggregation due to the dynamic nature of Aβ species and prolonged drug development cycles. Sensitive and real-time monitoring of Aβ structural transitions is therefore essential for understanding disease progression and evaluating potential inhibitors. In this study, we developed a ZIF-8-modified electrochemical biosensor capable of translating $Aβ_{42}$ conformational changes into quantifiable current signals, providing a promising platform for monitoring dynamic aggregation. The aggregation behavior of $Aβ_{42}$ was systematically characterized using dynamic light scattering (DLS), electrochemical measurements, and Thioflavin T (ThT) fluorescence combined with ultrafiltration. A critical transition from the lag to the growth phase was observed at 24 h, with aggregates exceeding ~60 nm undergoing irreversible fibrillization. The ZIF-8-modified electrochemical sensor detected early-stage structural rearrangements with superior sensitivity compared to conventional ThT fluorescence, revealing subtle oligomer formation. Quantitative current measurements allowed continuous monitoring of aggregation kinetics, highlighting the temporal resolution of the platform. Validation experiments with curcumin treatment demonstrated strong inhibitory effects between 18 and 24 h, delaying fibrillization, reducing late-stage β-sheet accumulation, and decreasing aggregate size by approximately 25%. In addition, the sensor successfully distinguished minor differences in structural transitions under varying inhibitor concentrations, demonstrating its capability for high-resolution, real-time assessment of aggregation dynamics and drug efficacy. This ZIF-8-modified electrochemical biosensor provides high-sensitivity, dynamic monitoring of $Aβ_{42}$ aggregation and drug-induced inhibition, offering a valuable tool for mechanistic studies of protein aggregation pathology. By enabling early detection of structural transitions and real-time evaluation of inhibitors, this platform has the potential to accelerate therapeutic screening and improve the development of effective interventions for AD.

Received 2nd February 2026
Accepted 11th April 2026

DOI: 10.1039/d6ra00907g

rsc.li/rsc-advances

1. Introduction

As global populations age, Alzheimer's disease (AD) has become a pressing public health challenge, with the World Alzheimer Report projecting 139 million dementia cases worldwide by 2050.[1] AD manifests as progressive memory loss, cognitive impairment, and behavioral changes, often accompanied by neuropsychiatric symptoms, placing significant burdens on patients and healthcare systems.[2] The disease's hallmarks include extracellular beta-amyloid (Aβ) plaques and intracellular neurofibrillary tangles formed by hyperphosphorylated tau protein [2]. These misfolded proteins act synergistically, driving synaptic dysfunction, neuroinflammation, and neural network disruption, with oxidative stress and inflammatory pathways implicated in their formation.[3] Elucidating Aβ aggregation dynamics is essential for understanding AD's neurodegenerative progression and developing effective therapeutics.

Aβ aggregation is a complex, multistep process involving transitions from monomers to soluble oligomers, protofibrils, and insoluble fibrils. Soluble oligomers and protofibrils, rather than mature fibrils, are now recognized as the primary neurotoxic species, disrupting neuronal function through mechanisms such as membrane pore formation, calcium

[a]*Department of Electronics and Electrical Engineering, National Yang Ming Chiao Tung University, Hsinchu City 300, Taiwan. E-mail: george@nycu.edu.tw*
[b]*Institute of Intelligent Bioelectrical Engineering, National Yang Ming Chiao Tung University, Hsinchu City 300, Taiwan*
[c]*College of Artificial Intelligence, National Yang Ming Chiao Tung University, Hsinchu City 300, Taiwan*
[d]*Catholic Mercy Hospital, Catholic Mercy Medical Foundation, Hsinchu County 303, Zhubei City, Taiwan*
[e]*Medical Device Innovation & Translation Center, National Yang Ming Chiao Tung University, Taipei City 112, Taiwan*
† Equal contribution.

dysregulation, and aberrant interactions with receptors like NMDAR and PrPc.[4–6] The aggregation follows a sigmoidal kinetic profile, with primary nucleation initiating oligomer formation, followed by rapid fibril elongation and secondary nucleation that amplifies toxic species.[7,8] Off-pathway oligomers, which are structurally stable, exhibit significant neurotoxicity, underscoring the need for sensitive detection methods to capture these early intermediates.[9,10] However, detecting these dynamic, heterogeneous species remains challenging due to their transient nature and structural diversity.

Thioflavin T (ThT) fluorescence assays are a standard tool for monitoring Aβ aggregation, leveraging their sensitivity to β-sheet structures in fibrils.[11,12] Yet, ThT is less effective at detecting early oligomeric species and cannot distinguish aggregate size or morphology, limiting its ability to fully characterize aggregation dynamics.[13] To address these shortcomings, this study introduces a Zeolitic Imidazolate Framework-8 (ZIF-8)-modified electrochemical biosensing platform for real-time monitoring of Aβ conformational changes across monomers, oligomers, and fibrils. Among various metal–organic frameworks (MOFs), ZIF-8 was specifically selected as the sensing platform due to its exceptional chemical stability in aqueous environments and superior biocompatibility compared to carboxylate-based MOFs.[14] Unlike many MOFs that undergo rapid hydrolysis, the strong coordination between zinc ions and imidazolate ligands in ZIF-8 ensures structural integrity during prolonged incubation in physiological buffers.[15] Furthermore, ZIF-8 possesses a high surface area and well-defined microporosity, which facilitates the effective entrapment of biomolecules while minimizing non-specific adsorption. Recent studies have shown that the strategic integration of MOF-based materials, such as bimetallic Co@Ni-MOFs, can significantly enhance charge-transfer efficiency and provide robust electrochemical stability.[16] Qin *et al.* further demonstrated the versatility of ZIF-8 by developing dual-mode sensors that exploit the competitive coordination between Zn^{2+} ions and Aβ species, achieving a broad detection range of 10^{-5}–10^{2} μM with a limit of detection (LOD) of 0.5 μM. Their results highlight the capability of ZIF-8-based platforms to sensitively detect trace amounts of Aβ.[17] By leveraging these advantageous properties, ZIF-8 provides a stable scaffold for Aβ interaction, enabling high-sensitivity monitoring of the complex protein aggregation process.

By translating structural transitions into quantifiable current signals, our ZIF-8 platform exploits high surface area and efficient biomolecule immobilization to achieve high selectivity and sensitivity. The system also facilitates screening of therapeutic candidates, such as curcumin, which inhibits Aβ aggregation and promotes non-toxic oligomers through non-covalent interactions.[18,19] Validated with curcumin, the platform yielded distinct dynamic responses, demonstrating its potential as a robust tool for early-stage drug discovery and mechanistic studies of AD. This approach offers a promising translational strategy for identifying novel AD therapeutics and accelerating drug development timelines.

2. Materials and methods

2.1. Chemicals

2-Methylimidazole, zinc nitrate hexahydrate, potassium hexacyanoferrate (II) ($K_4[Fe(CN)_6]$), potassium hexacyanoferrate (III) ($K_3[Fe(CN)_6]$), potassium chloride, and curcumin (98%) were purchased from Sigma-Aldrich (Darmstadt, Germany). Phosphate-buffered saline (1× PBS) was obtained from Fisher Scientific (Waltham, MA, USA). Dimethyl sulfoxide (DMSO, 99.9%) was purchased from JT Baker (Radnor, PA, USA). Thioflavin T (ThT, 95%) was purchased from Acros Organics (Geel, Belgium). 1,1,1,3,3,3-Hexafluoro-2-propanol (HFIP, 98%) was obtained from Matrix Scientific (Columbia, SC, USA). Human β-amyloid 1–42 peptide (DA-42, lyophilized powder, purity 96.45%) was purchased from Abcam (Cambridge, UK).

2.2. Instruments

Electrochemical measurements were performed using a Palmsens 4 electrochemical station (Palmsens, Netherlands) with screen-printed carbon electrodes (SPCE, TE100, Zensor, Taiwan). Dynamic light scattering (DLS) was carried out with an Anton Paar Litesizer 700 (Austria). Fluorescence measurements were obtained using a spectrometer (RF-6000, Shimadzu, Japan). An orbital shaker (TS-500D, Yihder, Taiwan) was used for incubating the samples. For purification, Microsep Advance centrifugal devices (10 K Omega, Pall Corporation, USA) were employed. The morphology of the samples was observed using a field-emission scanning electron microscope (FE-SEM, JSM-7401F, JEOL Ltd, Tokyo, Japan) operated at 5 kV with a working distance of 6 mm. Functional group composition was performed using FTIR-4600 Fourier-transform infrared spectroscopy (FTIR) from JASCO Corporation (Tokyo, Japan).

2.3. Preparation of Aβ monomers

Lyophilized $Aβ_{42}$ (1.5 mg) was dissolved in HFIP to a final concentration of 1 mg mL^{-1} and incubated overnight at 4 °C to ensure complete monomerization. The solution was then purged with nitrogen and vacuum-dried, leaving a transparent peptide film on the inner wall of the Eppendorf tube. This film was redissolved in 2.2 mM DMSO to 0.5 mg mL^{-1} and sonicated for 10 min. After centrifugation (10 000 rpm, 5 min, 4 °C) to remove insoluble aggregates, the supernatant was collected and diluted with 1× PBS to prepare a 100 μM $Aβ_{42}$ stock solution. 10 μM $Aβ_{42}$ was freshly prepared in 1× PBS before experiments, while aliquots of the remaining solution were stored at −20 °C and used within two weeks.

2.4. Time-dependent incubation and fractionation of $Aβ_{42}$

Eight tubes of $Aβ_{42}$ solution were incubated at 37 °C for 0, 12, 18, 24, 30, 36, 42, and 48 h. At each time point, 2–4 mL of solution was transferred into a 10 kDa MWCO ultrafiltration centrifugal device and centrifuged at 6690 rpm for 30–40 min at 4 °C. The ultrafiltration device enables rapid sample processing under mild conditions, preserving protein activity and conformation. Following centrifugation, the supernatant (macromolecular

species) and filtrate (low-molecular-weight components) were collected separately for subsequent experiments.

2.5. Time-dependent incubation and fractionation of curcumin-Aβ$_{42}$

For curcumin-treated samples, 10 μM curcumin was added after incubation, followed by another 24 h incubation at 37 °C. The samples were then processed using 3 kDa MWCO ultrafiltration devices (4 °C, 5000 rpm, 30 min) to remove free curcumin. Subsequent purification and fractionation were performed as in Section 2.4.

2.6. ZIF-8 synthesis

A 2.5 M 2-methylimidazole solution and a 25 mM zinc nitrate solution were prepared in deionized water. The two solutions were rapidly mixed and shaken at room temperature (105 rpm) for 30 min. The resulting milky suspension was centrifuged at 6000 rpm for 5 min, and the pellet was washed twice with deionized water. The obtained ZIF-8 nanoparticles were used immediately after synthesis.

2.7. Electrode preparation and electrochemical measurements

The SPCE was first rinsed with deionized water and dried. 3 μL of ZIF-8 (1 mg mL^{-1}) suspension was drop-cast onto the working electrode surface, evenly spread, and then dried under a fume hood for 30 minutes. Subsequently, 20 μL of pretreated Aβ$_{42}$ solution was drop-cast onto the WE and incubated at room temperature for 30 min. The electrode was then rinsed with 1× PBS and dried before electrochemical tests.

The potential window of differential pulse voltammetry (DPV) was set from −1.0 to 1.0 V, with a step size of 0.01 V. Pulses were applied with an amplitude of 50 mV and a duration of 0.1 s, and the scan rate was maintained at 5 mV s^{-1}. The electrochemical impedance spectroscopy (EIS) conditions included a direct current potential (E_{dc}) of 0.2 V, alternating current amplitude (E_{ac}) of 0.05 V, a frequency scan type, 40 frequencies (6.8 per decade), a maximum frequency of 80 000 Hz, and a minimum frequency of 0.2 Hz.

2.8. Dynamic light scattering (DLS) and fluorescence measurements

Aβ$_{42}$ solutions were incubated at 37 °C for designated time points (0–48 h). For DLS analysis, particle size distribution and aggregation were measured with 3 mL of sample in triplicate at 25 °C. For fluorescence measurements to monitor Aβ$_{42}$ aggregation kinetics, 3 mL aliquots—with or without 10 μM curcumin—were mixed with 20 μM ThT at a 1 : 19 volume ratio and protected from light.

3. Results and discussions

3.1. Characterization of ZIF-8 and modified electrodes

ZIF-8, which has the sodalite topology, typically forms truncated rhombic dodecahedra with hexagonal facets.[20] Freshly prepared ZIF-8, as shown in Fig. 1(a), appeared densely and uniformly distributed, though some regions showed higher particle density. Most particles exhibit well-defined polyhedral morphologies with sharp edges and, in some cases, distinct hexagonal shapes. In contrast, Fig. 1(b) reveals blurred edges after restoration, less distinct morphologies, and an increase in particle size (0.331–0.505 μm), indicating instability in deionized water that may cause precipitation over time. Such effects are strongly influenced by solvent choice and precursor ratios during synthesis.[21,22] Therefore, freshly prepared ZIF-8 synthesized in deionized water under the optimized formulation was used for subsequent experiments.

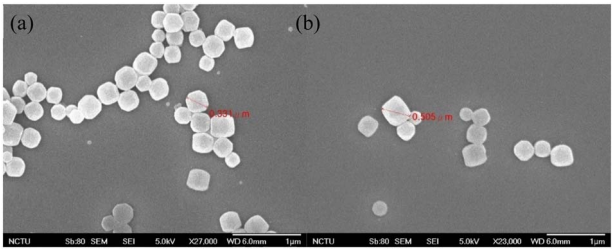

Fig. 1 SEM images of ZIF-8 particles: (a) freshly prepared and (b) after storage for 1 day post-synthesis.

FTIR was applied to investigate the formation of ZIF-8. Analysis of ZIF-8 revealed an adsorption band at 1575 cm^{-1} (C═N stretch) and two additional bands at 1422 cm^{-1} and 996 cm^{-1} (C–N stretch) (Fig. 2(a)), which are identical to those reported in previous research.[23] EIS confirmed the successful modification of ZIF-8 on the electrode surface. Compared with the bare electrode, the ZIF-8-modified electrode showed a slight increase in resistance (Fig. 2(b)), which did not affect the sensitivity of subsequent protein dynamics measurements.

3.2. Time-dependent size evolution and heterogeneity of Aβ$_{42}$ aggregates

Previous studies with highly oriented pyrolytic graphite (HOPG) electrodes showed that electroactive residues, such as Tyr10, produce an oxidation signal near +0.6 V.[24,25] However, reliance on natural peptide adsorption often causes overlap with the oxygen signal at +0.8 V, making the measurements prone to background interference and highly dependent on strict sample and electrode preparation. To address these issues, this study employed a ZIF-8-modified SPCE, which offers stable adsorption across Aβ$_{42}$ conformations, minimizes background interference, and facilitates real-time monitoring of aggregation dynamics.

Fig. 3(a) and (b) indicate the relationship between the incubation time and the DPV curves. With increasing incubation time, the oxidation peak current near 0 V for Aβ$_{42}$ decreased from 14.554 μA at 0 h to 11.859 μA at 48 h, with all relative standard deviations (RSDs) remaining below 8%. This decline reflects the reduction of monomers and low-order oligomers, as larger aggregates form. During this process, the aggregated Aβ$_{42}$ structures form a thicker and more continuous insulating protein layer on the electrode surface. This dense layer reduces

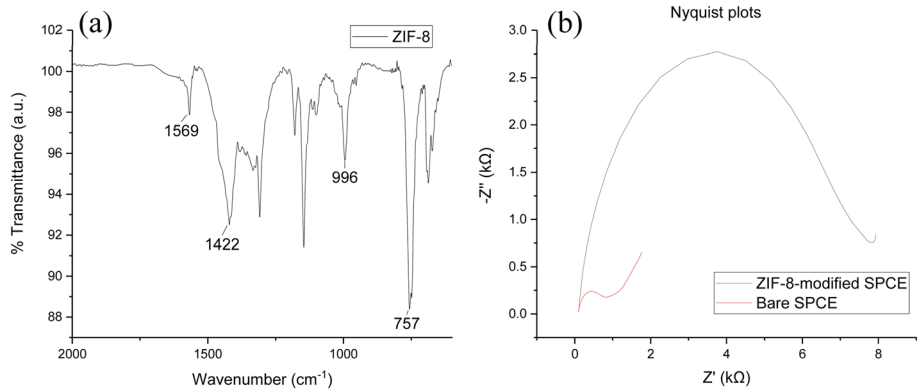

Fig. 2 (a) FTIR spectrum of ZIF-8. (b) Impedance plots for (red) bare electrodes and (black) ZIF-8-modified SPCEs.

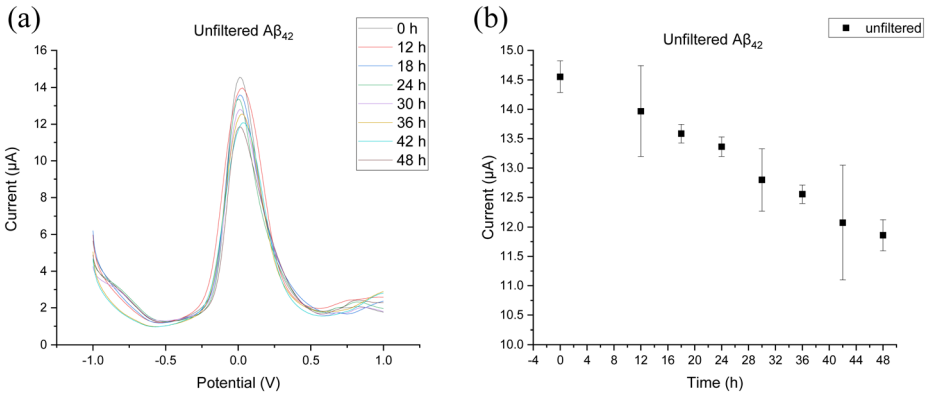

Fig. 3 Time-dependent decline of $A\beta_{42}$ peak current: (a) DPV curves and (b) corresponding peak values and error bars.

the electron-transfer efficiency of the charged redox probe molecules, resulting in a progressive decrease in current as the degree of aggregation increases.[25–27]

In contrast, DLS measurements (Fig. 4) revealed a particle size range of ~100 to >400 nm over 0–48 h, with the average size at 24 h (411.18 nm) exceeding that at 48 h (235.31 nm). Since later-stage fibrillization is expected to yield the largest aggregates, this unexpected trend suggests aggregation heterogeneity. Full-width at half maximum (FWHM) values further support this: the distribution was sharp at 0 h (0 nm), broadened slightly at 12 h (11.19 nm), and became bimodal at 24 h (58.9 nm), consistent with the coexistence of oligomers and protofibrils. At 48 h, heterogeneity peaked (69.6 nm), reflecting a mixture of diverse aggregate populations.

These findings reveal that $A\beta_{42}$ aggregation follows heterogeneous pathways: some species form large fibrils with low electrochemical activity, while others persist as smaller, more active oligomers. This heterogeneity obscures direct correlations between bulk size and electrochemical response. To address this, we applied a simple purification strategy using a 10 kDa MWCO centrifugal device, separating the supernatant (larger aggregates) from the filtrate (smaller species). This fractionation enabled size-dependent electrochemical analysis, providing clearer resolution of aggregation heterogeneity.[28]

3.3. $A\beta_{42}$ supernatant analysis

The resulting supernatant, enriched in oligomeric and aggregated species larger than 10 kDa, was analyzed. Fig. 5(a) and (b)

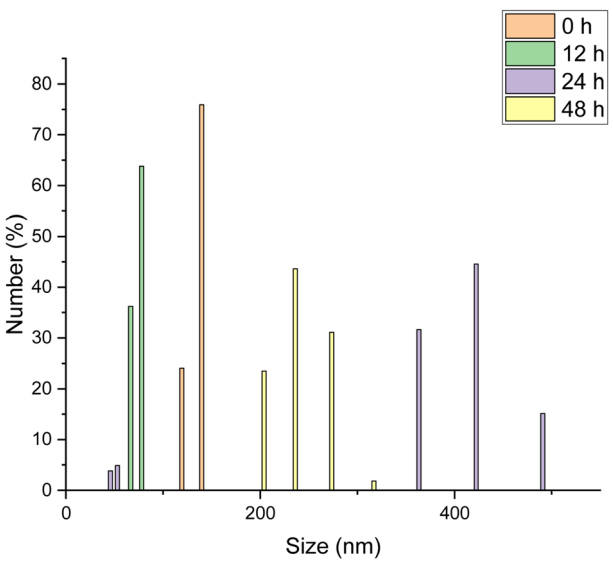

Fig. 4 Time-dependent particle size distribution of $A\beta_{42}$ measured by DLS. Size evolution from 0 h to 48 h is 141.17, 75.83, 411.18, and 235.31 nm.

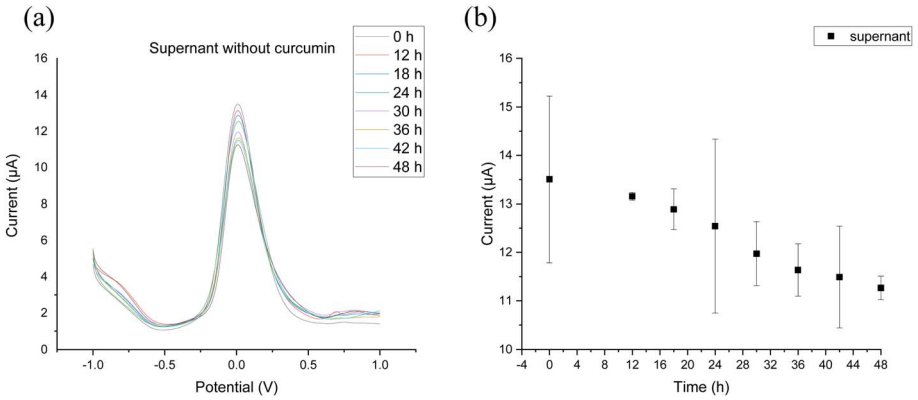

Fig. 5 Time-dependent decline of $A\beta_{42}$ supernant peak current: (a) DPV curves and (b) corresponding peak values.

present the DPV current-potential responses and the correlation between average current values and incubation time. The peak current was highest at 0 h (13.505 μA), decreased slightly by 12 h (13.152 μA), and dropped further at 24 h (12.542 μA), reaching 11.27 μA at 48 h, confirming the continuous progression of aggregation.

During early incubation (0–12 h), oligomeric species predominated. $A\beta_{42}$ monomers and small oligomers adsorb onto the ZIF-8, forming a thin and loosely packed protein layer, which results in higher current responses. As aggregation progresses, the formation of larger assemblies increases steric hindrance and reduces diffusion, thereby impeding the approach of the $[Fe(CN)_6]^{3-/4-}$ redox probe and further restricting electron transfer, leading to a decrease in current intensity.[24,26,27]

Notably, Fig. 5(b) exhibits a pronounced increase in the error bar at 24 h. This time point corresponds to the critical nucleation phase of $A\beta_{42}$ aggregation, during which species with diverse sizes and conformations coexist, resulting in maximal heterogeneity.[29] At this stage, the supernatant displayed substantial variability: in some replicates, electroactive oligomeric species with relatively high surface accessibility predominated, whereas in others, larger post-nucleation aggregates were more prevalent. Once the nucleation threshold was exceeded, stochastic fluctuations in aggregate composition and size became apparent, leading to reduced reproducibility of the DPV current and enlarged error bars—characteristic features of the critical aggregation phase. Although the absolute differences in DPV peak currents are moderate and accompanied by increased variability at specific time points, the platform consistently captures aggregation-dependent trends and reliably identifies the critical transition phase of $A\beta_{42}$ assembly.

Analysis of the overall trend revealed distinct current behaviors across three time intervals: 0–24 h (slope = −0.039), 24–36 h (slope = −0.076), and 36–48 h (slope = −0.031). The most pronounced change occurred during the second interval, which corresponds to the critical phase of $A\beta_{42}$ oligomer nucleation and aggregation. This observation is consistent with the proposed mechanism, in which progressive aggregation reduces the redox probe's accessibility to the electrode surface, thereby attenuating electron transfer. Supporting this interpretation, DLS measurements exhibited a slope of 0.973 in the first interval and a markedly higher slope of 7.985 in the second interval, indicating accelerated growth and increased heterogeneity during the nucleation stage.

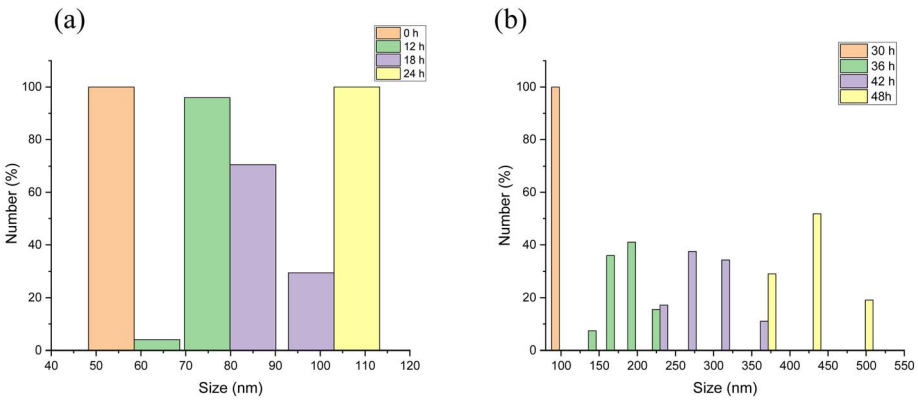

Fig. 6 Time-dependent particle size distribution of $A\beta_{42}$ supernatant measured by DLS. Size (nm) evolution from (a) 0 h to 24 h is 68.69, 79.43, 83.72, and 92.98, and (b) 30 h to 48 h is 108.03, 188.80, 286.10, and 416.13.

The corresponding size averages are summarized in Fig. 6(a) and (b). In the early stage (0–30 h), the size distribution remained narrow (68.69–108.03 nm). This phase corresponds to the lag stage of aggregation, characterized by the presence of soluble monomers and low-order oligomers undergoing initial nucleation.[28,30,31] These species are generally considered the most neurotoxic forms, owing to their ability to penetrate cell membranes or interact with cellular receptors.[5,32]

In contrast, after 36 h, a broad peak appeared, marking the growth phase where nuclei exceeding the critical size drive rapid aggregation.[30,31] By 42–48 h, species >300 nm predominated, indicating accelerated assembly into large oligomers and fibrils,[33] highlighting the time-dependent progression of $A\beta_{42}$ aggregation. These larger aggregates, although structurally stable, are often less toxic because the surface area available for direct cellular interactions is reduced.

In summary, the assessment of a candidate compound's ability to inhibit or promote the degradation of $A\beta_{42}$ aggregation can be effectively determined by analyzing the changes in electrochemical current during the 24–36 h incubation window, as will be further examined in the subsequent curcumin experiments.

3.4. $A\beta_{42}$ filtrate analysis

DPV analysis was conducted on the filtrate, which contains molecular species smaller than 10 kDa. Fig. 7(a) and (b) present the current-potential response and the correlation between average current and incubation time, respectively. The primary oxidation peak exhibited a nonlinear "rise-fall" trend: the current was relatively low at 0 h (11.60 μA), increased at 12 h (13.73 μA), and reached a maximum at 24 h (14.27 μA). This biphasic behavior indicates that prior to 24 h, events are primarily attributed to the dissociation of pre-existing low-molecular-weight oligomers or unstable aggregates, releasing more monomers and small oligomers with enhanced conformational flexibility and greater exposure of electroactive residues allow the assemblies to retain greater conformational flexibility and to bind stably to ZIF-8, forming an interface that facilitates electron transfer of the $[Fe(CN)_6]^{3-/4-}$ redox probe and thereby enhances the DPV response. In contrast, after 24 h, structural reorganization leads to more compact and less accessible assemblies, which begin to hinder probe diffusion and consequently reduce electron-transfer efficiency, resulting in lower currents. In contrast, the supernatant exhibited a monotonic decline in current, indicating that sub-10 kDa species in the filtrate serve as critical transitional intermediates in $A\beta_{42}$ aggregation.

The 24 h time point corresponds to the critical transition between reversible early-stage dynamics and the irreversible formation of higher-order assemblies. This stage also coincides with the heightened heterogeneity and polymorphism observed in the supernatant, as evidenced by DLS measurements (Fig. 8(a) and (b)), underscoring its pivotal role in the aggregation pathway.

Moreover, the results suggest that $A\beta_{42}$ oligomers preferentially adsorb to ZIF-8 due to the exposed functional groups. Monomers exhibit only partial adsorption, while fibrils—with residues largely buried within rigid aggregates—interact minimally with ZIF-8. The higher surface accessibility and dynamic conformations of oligomers confer a larger effective binding constant, explaining why DPV signals from certain filtrates may be lower than those of the corresponding supernatants, reflecting the selective contribution of oligomeric species.[34,35]

3.5. Analysis of curcumin-mediated structural degradation in the supernatant

Fig. 9 compares the electrochemical responses of the $A\beta_{42}$-only system (blue) and the $A\beta_{42}$ + curcumin system (orange), in which curcumin was removed prior to measurement. The $A\beta_{42}$ + curcumin system consistently exhibited higher current values than $A\beta_{42}$ alone, with the most pronounced differences observed between 12 and 24 h. During this interval, the current variations were 1.154, 1.909, and 1.264 μA for 12, 18, and 24 h, respectively, indicating that curcumin most effectively interfered with $A\beta_{42}$ nucleation in this phase. By hindering the formation of toxic oligomers and fibrils, curcumin reduced the complexity and heterogeneity of subsequent aggregation. After 24 h, although the current values of the curcumin-treated system remained higher than the $A\beta_{42}$-only group, its relative inhibitory effect became less pronounced.

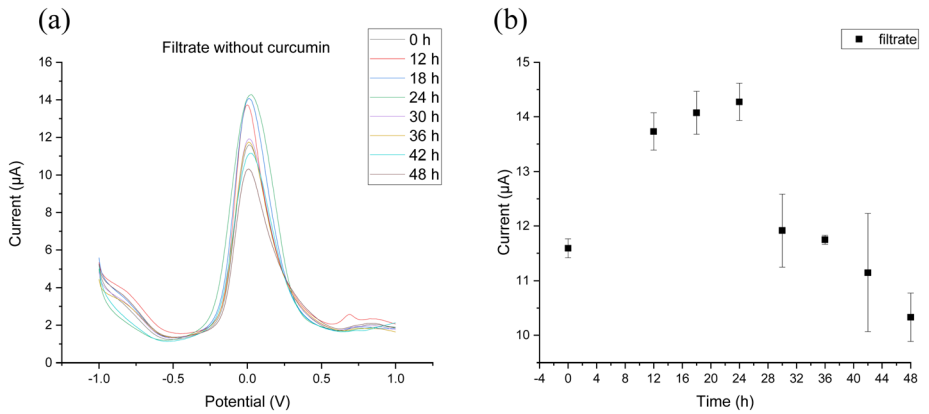

Fig. 7 Time-dependent decline of $A\beta_{42}$ filtrate peak current: (a) DPV curves and (b) corresponding peak values.

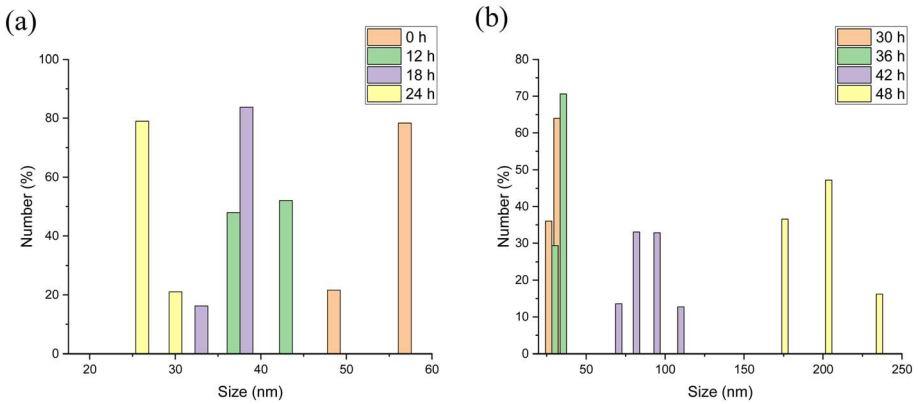

Fig. 8 Time-dependent particle size distribution of $A\beta_{42}$ filtrate measured by DLS. Size (nm) evolution from (a) 0 h to 24 h is 57.28, 40.74, 36.70, and 24.70, and (b) 30 h to 48 h is 35.66, 36.01, 86.76, and 192.66.

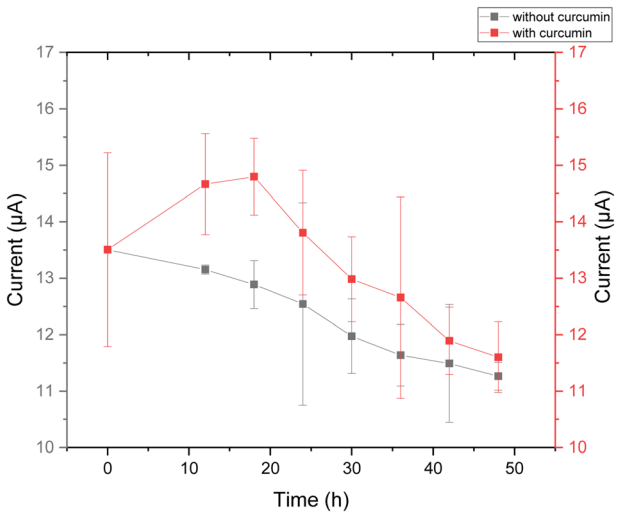

Fig. 9 Current difference between (black) $A\beta_{42}$-only and (red) curcumin-$A\beta_{42}$ supernatant.

Comparative validation using DLS, electrochemical, and fluorescence analyses identified 24 h as a critical turning point in the aggregation process, marking the onset of the growth phase in $A\beta_{42}$ kinetics. The most pronounced current differences between 18 and 24 h likely correspond to the transition from the late lag phase to the early growth phase. In other words, the 12–18 hour interval should be highlighted as an "optimal intervention window" for inhibitory compounds, as the current change from baseline could differentiate the ability to inhibit core generation. As the aggregation process approaches 24 h, during which higher drug concentrations or stronger disaggregation capacity may be required. Moreover, the enlarged current error suggests that structural complexity has markedly increased, rendering pharmacological intervention less effective than in the earlier, more stable stage.

These observations are consistent with previous studies reporting that curcumin exerts its strongest inhibitory effect on $A\beta_{40/42}$ aggregation within 24 h.[36] This activity is generally attributed to π–π stacking and hydrogen-bonding interactions between phenolic rings and peptide backbones, which confer anti-aggregation properties.[37] Mechanistically, curcumin can target β-sheet assemblies in secondary structures, disrupting or dissociating β-sheets on fibril surfaces, thereby reducing fibril stability and blocking elongation. Alternatively, curcumin may insert into fibril structures, perturb their organization, or induce disorder in peripheral peptide segments, thereby hindering the recruitment of new Aβ monomers.[38,39]

Fig. 10 shows the ThT fluorescence intensity (485 nm) of $A\beta_{42}$ in the supernatant during different incubation times. In the $A\beta_{42}$-only system, fluorescence increased steadily from 1337.76 a.u. at 12 h to 1618.06 a.u. at 48 h, reflecting continuous β-sheet fibril formation. In contrast, the $A\beta_{42}$ + curcumin system showed consistently lower values (1250.48–1336.04 a.u), indicating that curcumin interfered with monomer incorporation into fibrils. This early inhibition suppressed β-sheet accumulation at later stages, resulting in a clear divergence in fluorescence during the 36–48 h, the late aggregation phase.

Combined with electrochemical data, the ThT results confirm that curcumin delays $A\beta_{42}$ fibrillization, maintaining

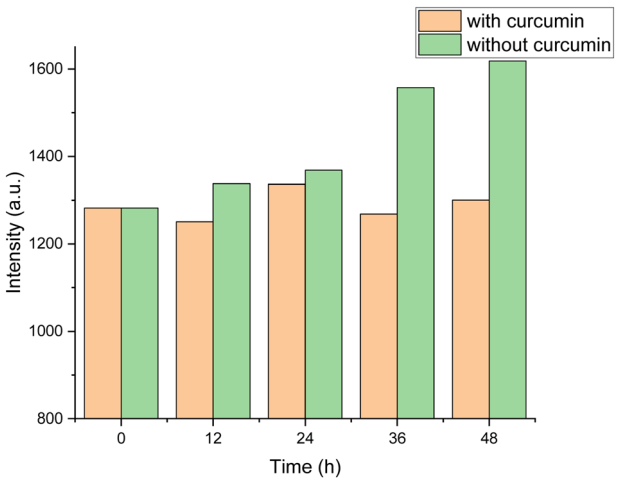

Fig. 10 Fluorescence intensity difference between (green) $A\beta_{42}$-only and (orange) curcumin-$A\beta_{42}$ supernatant.

higher electrochemical activity while reducing β-sheet-associated fluorescence.

3.6. Analysis of curcumin-mediated structural degradation in the filtrate

As shown in Fig. 11, for $A\beta_{42}$ filtrate alone, the initial current was 11.591 μA, gradually increasing from 12 to 24 h, indicative of dissociation into smaller species, and subsequently declining after 30 h, suggesting reaggregation. In the curcumin-treated filtrates, current values were higher at 12–24 h, with the maximum variation observed at 18 h, though decreased during 30–36 h, remaining above those of $A\beta_{42}$ alone.

The inhibitory effect of curcumin was most evident between 12 and 30 hours, consistent with trends observed in the supernatant, particularly the greatest current change at 18 hours.

Fig. 12 presents the ThT fluorescence intensity (485 nm) change. In the $A\beta_{42}$-alone group, fluorescence intensity decreased up to 24 h, suggesting partial structural dissociation, but rose again from 36–48 h, reflecting re-aggregation into short oligomers rather than large β-sheet fibrils. In contrast, the $A\beta_{42}$ + curcumin system consistently exhibited lower fluorescence values, indicating reduced β-sheet formation. Together, these results show that the filtrates mainly contained monomers and small oligomers with limited β-sheet content, and that curcumin further disrupted β-sheet assembly, thereby hindering the progression of low-molecular-weight species into higher-order aggregates.[40]

3.7. Comparative insights and translational implications

In this study, the time-dependent decrease in DPV peak current is best explained by the gradual formation of a compact, insulating protein layer on the ZIF-8-modified electrode surface. As $A\beta_{42}$ assemblies evolve, key electroactive residues, such as Tyr, His, and Met, become progressively buried within higher-order

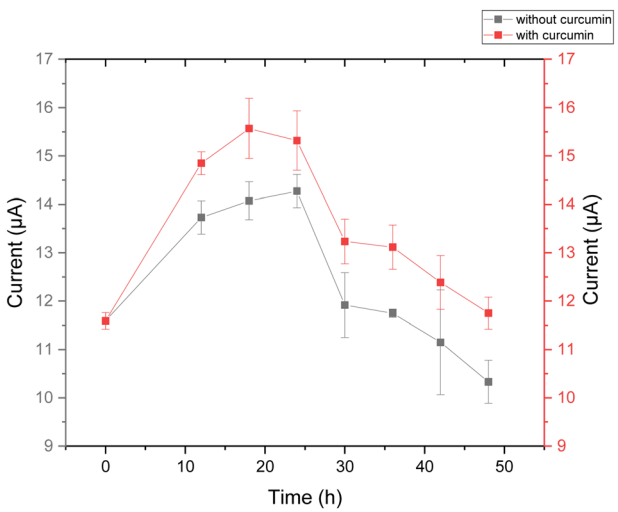

Fig. 11 Current difference between (black) $A\beta_{42}$-only and (red) curcumin-$A\beta_{42}$ filtrate.

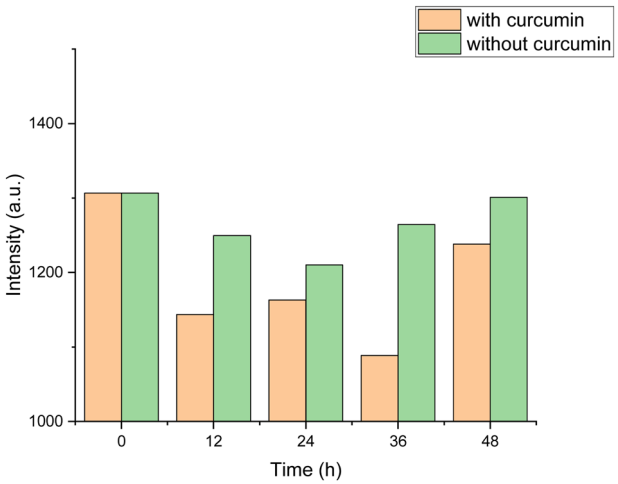

Fig. 12 Fluorescence intensity difference between (green) $A\beta_{42}$-only and (orange) curcumin-$A\beta_{42}$ filtrate.

aggregates, thereby diminishing their contribution to interfacial electron transfer. Concurrently, DLS measurements show a marked increase in hydrodynamic size—exceeding 60 nm after the critical 24 h transition—which further restricts the diffusion of larger assemblies to the electrode interface. These observations are consistent with established protein-film electrochemical behavior, where conformational compaction and reduced surface mobility suppress faradaic responses. Curcumin intervention provides additional mechanistic support: samples treated with curcumin exhibit significantly higher currents between 18–24 h and reduced ThT fluorescence, indicating attenuated β-sheet formation and less densely packed surface films (Fig. 13). Moreover, given prior reports that ZIF-8 preferentially adsorbs oligomeric Aβ species, the enhanced early-stage signal modulation is likely driven by selective surface enrichment of aggregation-competent intermediates, which accelerates subsequent physical blocking. Taken together, these results suggest that the dominant contributor to current suppression is steric and structural in nature—arising from the accumulation of compact, diffusion-limiting aggregates—rather than a mechanism governed primarily by electrostatic perturbation of the redox probe.

The distinct electrochemical responses of the filtrate (<10 kDa) and supernatant (>10 kDa) arise from differences in size, secondary structure, and residue accessibility. The filtrate, enriched in monomers and small oligomers, is structurally dynamic and adopts random coil or β-turn conformations, leaving electroactive residues (Tyr10, His6, His13, His14, Met35) exposed. These species diffuse efficiently to the ZIF-8 electrode and, owing to higher hydrophobicity, enhance adsorption and electron transfer. As a result, filtrate currents rise until ~24 hours, then decline due to higher-order aggregation. In contrast, the supernatant contains larger oligomers and protofibrils with β-sheet-rich conformations, in which electroactive residues are buried and steric hindrance limits electrode contact, leading to a steady decline in current. This disparity underscores the ZIF-8 platform's sensitivity to early

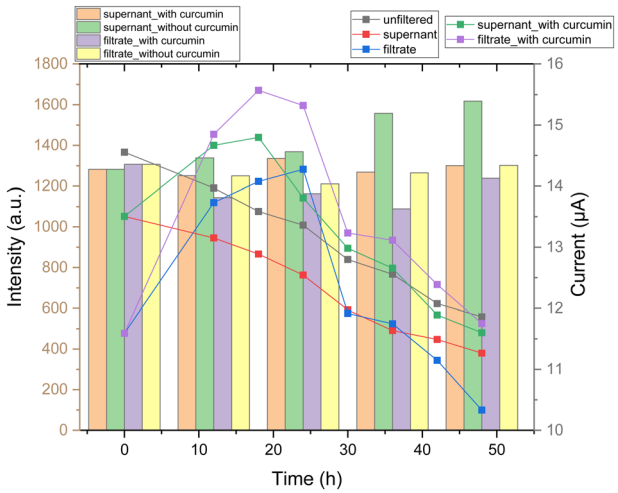

Fig. 13 Comparison of the electrochemical and fluorescence results. Both measurements indicate that effective intervention must occur before the 24-hour transition point, with the optimal window identified at 12–18 hours.

intermediates. Moreover, the supernatant provides a more reliable monitoring target, as its monotonic current decrease correlates well with aggregation and allows for clearer discrimination of drug effects, as demonstrated by curcumin inhibition. We therefore recommend prioritizing the supernatant for future applications, given its stable and discriminative electrochemical behavior in evaluating $A\beta_{42}$ modulators.

In summary, the ZIF-8-based core–shell platform enables electrochemical monitoring of $A\beta_{42}$ aggregation by transducing the peptide's structural evolution into measurable interfacial electron-transfer changes. While the system can distinguish different aggregation states, its selectivity toward $A\beta_{42}$ remains constrained by the nonspecific adsorption and size-dependent partitioning processes that dominate the current sensing mechanism. These limitations may hinder reliable operation in complex biological matrices. To advance this platform toward more analytically robust applications, integrating defined bio-recognition motifs at the ZIF-8 interface will be essential. In future work, molecular imprinting or other selective recognition strategies could be incorporated to enhance binding specificity and selectivity,[41] thereby supporting the development of modular and potentially portable sensing formats.

4. Conclusion

This study demonstrates that the ZIF-8-modified SPCE platform provides a robust, reproducible, and cost-effective method for monitoring $A\beta_{42}$ aggregation and evaluating the effects of inhibitory compounds, such as curcumin. Aggregation exhibits time-dependent heterogeneity: low-molecular-weight species dominate early with high electrochemical activity, while larger aggregates reduce electrode accessibility at later stages. The 24-hour mark represents a critical transition, with an optimal intervention window at 12–18 h, during which curcumin effectively delays β-sheet formation and fibrillization. Unlike antibody- or aptamer-based biosensors designed for clinical sample detection, this platform prioritizes rapid and high-throughput drug screening. SPCE electrodes enable scalability for array fabrication, and the straightforward synthesis of ZIF-8 ensures reproducibility and consistency, facilitating the exploration of large-scale potential $A\beta_{42}$ oligomer inhibitors. Together, these features position the platform as a valuable tool for early-phase drug discovery, which can be integrated with clinical detection data to accelerate the development of AD therapeutics.

Author contributions

Methodology and writing – original draft: Shang-Chi Chien and Yin-Chen Chein. Data analysis: Hung-Ju Wang. Resources, conceptualization, and supervision: Jung-Chin Chen.

Conflicts of interest

The authors declare that they have no conflicts of interest.

Data availability

The data supporting the findings of this study are available upon request from the corresponding author.

Acknowledgements

In preparing this study, the authors used ChatGPT 5 and Grok 4 to enhance readability. After using this tool/service, the authors reviewed and edited the content as necessary and assumed full responsibility for the study's content. This study was partially funded and supported by the National Science and Technology Council (NSTC 114-2221-E-A49-090, NSTC 114-2321-B-A49-002, NSTC 114-2640-B-A49-001) of Taiwan.

References

1 S. Evans-Lacko, *et al.*, *World Alzheimer Report 2024. Global Changes in Attitudes to Dementia*. Alzheimer's Disease International, 2024.
2 J. Gallego-Rudolf, *et al.*, Synergistic association of Abeta and tau pathology with cortical neurophysiology and cognitive decline in asymptomatic older adults, *Nat. Neurosci.*, 2024, **27**(11), 2130–2137.
3 V. Bhatia and S. Sharma, Role of mitochondrial dysfunction, oxidative stress and autophagy in progression of Alzheimer's disease, *J. Neurol. Sci.*, 2021, **421**, 117253.
4 H. Hampel, *et al.*, The Amyloid-beta Pathway in Alzheimer's Disease, *Mol. Psychiatr.*, 2021, **26**(10), 5481–5503.
5 X. Meng, *et al.*, Neurotoxic beta-amyloid oligomers cause mitochondrial dysfunction-the trigger for PANoptosis in neurons, *Front. Aging Neurosci.*, 2024, **16**, 1400544.
6 M. M. Rahman and C. Lendel, Extracellular protein components of amyloid plaques and their roles in Alzheimer's disease pathology, *Mol. Neurodegener.*, 2021, **16**(1), 59.

7 D. J. Rinauro, *et al.*, Misfolded protein oligomers: mechanisms of formation, cytotoxic effects, and pharmacological approaches against protein misfolding diseases, *Mol. Neurodegener.*, 2024, **19**(1), 20.
8 P. Arosio, T. P. Knowles and S. Linse, On the lag phase in amyloid fibril formation, *Phys. Chem. Chem. Phys.*, 2015, **17**(12), 7606–7618.
9 G. F. Chen, *et al.*, Amyloid beta: structure, biology and structure-based therapeutic development, *Acta Pharmacol. Sin.*, 2017, **38**(9), 1205–1235.
10 S. I. Cohen, *et al.*, Proliferation of amyloid-beta42 aggregates occurs through a secondary nucleation mechanism, *Proc. Natl. Acad. Sci. U. S. A.*, 2013, **110**(24), 9758–9763.
11 C. Xue, *et al.*, Thioflavin T as an amyloid dye: fibril quantification, optimal concentration and effect on aggregation, *R. Soc. Open Sci.*, 2017, **4**(1), 160696.
12 H. LeVine, Thioflavine T interaction with synthetic Alzheimer's disease beta-amyloid peptides: detection of amyloid aggregation in solution, *Protein Sci.*, 1993, **2**(3), 404–410.
13 M. D'Amico, *et al.*, Thioflavin T Promotes Abeta(1-40) Amyloid Fibrils Formation, *J. Phys. Chem. Lett.*, 2012, **3**(12), 1596–1601.
14 K. S. Park, *et al.*, Exceptional chemical and thermal stability of zeolitic imidazolate frameworks, *Proc. Natl. Acad. Sci. U. S. A.*, 2006, **103**(27), 10186–10191.
15 L. B. Shano, *et al.*, MOFs for next-generation cancer therapeutics through a biophysical approach—a review, *Front. Bioeng. Biotechnol.*, 2024, **12**, 1397804.
16 M. Sivakumar, *et al.*, Sphere-like Co-doped Ni metal-organic framework for enhanced oxygen evolution reaction, *J. Phys. Chem. Solids*, 2025, **207**, 112918.
17 J. Qin, M. Cho and Y. Lee, Ferrocene-encapsulated zn zeolitic imidazole framework (ZIF-8) for optical and electrochemical sensing of amyloid-β oligomers and for the early diagnosis of alzheimer's disease, *ACS Appl. Mater. Interfaces*, 2019, **11**(12), 11743–11748.
18 P. B. Goncalves, Y. Cordeiro and A. C. Renno Sodero, Understanding the mechanisms of green tea EGCG against amyloid beta oligomer neurotoxicity through computational studies, *RSC Adv.*, 2024, **14**(31), 22525–22539.
19 C. Secker, *et al.*, The polyphenol EGCG directly targets intracellular amyloid-beta aggregates and promotes their lysosomal degradation, *J. Neurochem.*, 2023, **166**(2), 294–317.
20 M. Bergaoui, *et al.*, A review of the features and applications of ZIF-8 and its derivatives for separating CO2 and isomers of C3- and C4- hydrocarbons, *J. Nat. Gas Sci. Eng.*, 2021, **96**, 104289.
21 A. Akhundzadeh Tezerjani, R. Halladj and S. Askari, Different view of solvent effect on the synthesis methods of zeolitic imidazolate framework-8 to tuning the crystal structure and properties, *RSC Adv.*, 2021, **11**(32), 19914–19923.
22 M. Jian, *et al.*, Water-based synthesis of zeolitic imidazolate framework-8 with high morphology level at room temperature, *RSC Adv.*, 2015, **5**(60), 48433–48441.
23 X. Zeng, *et al.*, Sonocrystallization of ZIF-8 on electrostatic spinning TiO2 nanofibers surface with enhanced photocatalysis property through synergistic effect, *ACS Appl. Mater. Interfaces*, 2016, **8**(31), 20274–20282.
24 S. Seo, *et al.*, Electrical characteristics of amyloid beta peptides in vertical junctions, *NPG Asia Mater.*, 2021, **13**(1), 54.
25 T. A. Enache, A. M. Chiorcea-Paquim and A. M. Oliveira-Brett, Amyloid Beta Peptide VHHQ, KLVFF, and IIGLMVGGVV Domains Involved in Fibrilization: AFM and Electrochemical Characterization, *Anal. Chem.*, 2018, **90**(3), 2285–2292.
26 A. J. Veloso, *et al.*, Electrochemical immunosensors for effective evaluation of amyloid-beta modulators on oligomeric and fibrillar aggregation processes, *Anal. Chem.*, 2014, **86**(10), 4901–4909.
27 J. Sopoušek, *et al.*, Crucial factors governing the electrochemical impedance on protein-modified surfaces, *Electrochim. Acta*, 2021, **388**, 138616.
28 G. Bitan, *et al.*, amyloid-β-protein-(aβ)-assembly-aβ40-and-aβ42-oligomerize-through-distinct-pathways, *Proc. Natl. Acad. Sci. U. S. A.*, 2002, **100**(1), 330–335.
29 A. K. Srivastava, *et al.*, beta-Amyloid aggregation and heterogeneous nucleation, *Protein Sci.*, 2019, **28**(9), 1567–1581.
30 K. M. Saravanan, *et al.*, On the Conformational Dynamics of beta-Amyloid Forming Peptides: A Computational Perspective, *Front. Bioeng. Biotechnol.*, 2020, **8**, 532.
31 T. K. Karamanos, *et al.*, Mechanisms of amyloid formation revealed by solution NMR, *Prog. Nucl. Magn. Reson. Spectrosc.*, 2015, **88–89**, 86–104.
32 M. Ahmed, *et al.*, Structural conversion of neurotoxic amyloid-beta(1-42) oligomers to fibrils, *Nat. Struct. Mol. Biol.*, 2010, **17**(5), 561–567.
33 J. P. Dolle, *et al.*, Newfound effect of N-acetylaspartate in preventing and reversing aggregation of amyloid-beta in vitro, *Neurobiol. Dis.*, 2018, **117**, 161–169.
34 J. Qin, M. Cho and Y. Lee, Ferrocene-Encapsulated Zn Zeolitic Imidazole Framework (ZIF-8) for Optical and Electrochemical Sensing of Amyloid-beta Oligomers and for the Early Diagnosis of Alzheimer's Disease, *ACS Appl. Mater. Interfaces*, 2019, **11**(12), 11743–11748.
35 J. P. Leite, *et al.*, Metal-Organic Frameworks as Sensors for Human Amyloid Diseases, *ACS Sens.*, 2023, **8**(3), 1033–1053.
36 C. M. R. Madhuranthakam, A. Shakeri and P. P. N. Rao, Modeling the Inhibition Kinetics of Curcumin, Orange G, and Resveratrol with Amyloid-beta Peptide, *ACS Omega*, 2021, **6**(12), 8680–8686.
37 J. Lakey-Beitia, *et al.*, Assessment of Novel Curcumin Derivatives as Potent Inhibitors of Inflammation and Amyloid-beta Aggregation in Alzheimer's Disease, *J. Alzheimers Dis.*, 2017, **60**(s1), S59–S68.
38 F. Yang, *et al.*, Curcumin inhibits formation of amyloid beta oligomers and fibrils, binds plaques, and reduces amyloid in vivo, *J. Biol. Chem.*, 2005, **280**(7), 5892–5901.
39 J. M. Jakubowski, *et al.*, Interactions between Curcumin Derivatives and Amyloid-beta Fibrils: Insights from

Molecular Dynamics Simulations, *J. Chem. Inf. Model.*, 2020, **60**(1), 289–305.

40 I. Doytchinova, *et al.*, Curcumin Inhibits the Primary Nucleation of Amyloid-Beta Peptide: A Molecular Dynamics Study, *Biomolecules*, 2020, **10**(9), 1323.

41 T. Li, *et al.*, Preparation of artificial substrate binding sites of nanozyme with "modular structure" strategy used for the construction of visual sensing analysis platform for levodopa, *Microchem. J.*, 2025, **212**, 113292.